THE DEVELOPMENT OF WAVERIDERS USING AN AXISYMMETRIC FLOWFIELD

Frederick Ferguson, Terry Corbett and Haile Lindsay
Center for Aerospace Research
North Carolina A&T State University
Greensboro, NC, 27411

ABSTRACT

In this paper, waverider configurations are generated by specifying an arbitrary conical shockwave shape, and a corresponding leading edge. This inverse design approach makes use of a numerical tool which is based on a semi-analytical approach for solving the Euler equations. In the waverider design space, the aerodynamic figure of merit, (L/D) is considered a function of the shapes of both the conical shockwaves and leading edges. The waverider configuration and aerodynamic performance are considered functions of eight design parameters. The method yields practical vehicle shapes with acceptable volumetric efficiencies. The design method is computationally efficient and permits rapid parametric studies. Several viscous optimized waverider configurations were constructed and their aero performance analyzed. Results show that the waveriders created have acceptable L/D when compared to the Kuchemann Barrier, at times crossing it.

NOMENCLATURE

ß	=	shockwave angle
C_D	=	skin friction coefficient
C_L	=	pressure coefficient
D	=	Drag, force component parallel to the freestream velocity
L	=	Lift, force component perpendicular to the freestream velocity
L/D	=	Lift over drag ratio
M	=	Mach number
θ	=	wedge angle
p	=	pressure
q_∞	=	freestream dynamic pressure
S	=	Surface area
τ	=	shear stress
T	=	temperature
V_{eff}	=	volumetric efficiency

I. INTRODUCTION

A basic feature of all in-flight hypersonic vehicles is the creation of relatively strong shockwaves emanating from their leading edges. Associated with the flowfields behind these shockwaves are severe aerothermodynamics, propulsion system integration and aeroelastic design problems. This feature is characteristic of both ballistic and lifting vehicles, so in either case the relationship between shockwave shape and vehicle shape is of fundamental importance to effective vehicle design. After a thorough review of flight vehicle performance over a range of

Mach numbers, Kuchemann established an L/D barrier and the associated aircraft configurations that perform best with this barrier, Ref. 1. Kuchemann demonstrated in Figure 1 that at high Mach numbers in order to maximize aircraft performance, blended body configurations with tightly integrated forebodies, propulsion and nozzle afterbodies are favored. Later, Bowcutt, Ref. 2 showed not only that waverider configurations supported the Kuchemann findings, but that viscous optimized waverider configurations can potentially out-perform the blended body aircraft configurations and thus break the 'L/D barrier' Kuchemann established. Bowcutt's findings were later supported by others, Refs. 3 & 4 as demonstrated in the illustration depicted in Figure 2.

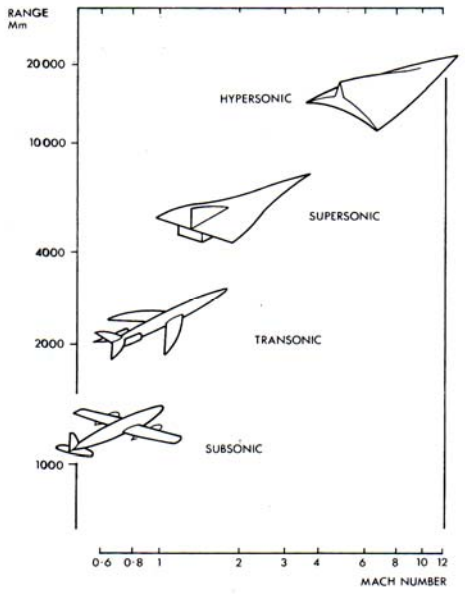

Figure 1: Influence of Flight Mach number and Performance on Aircraft Shape

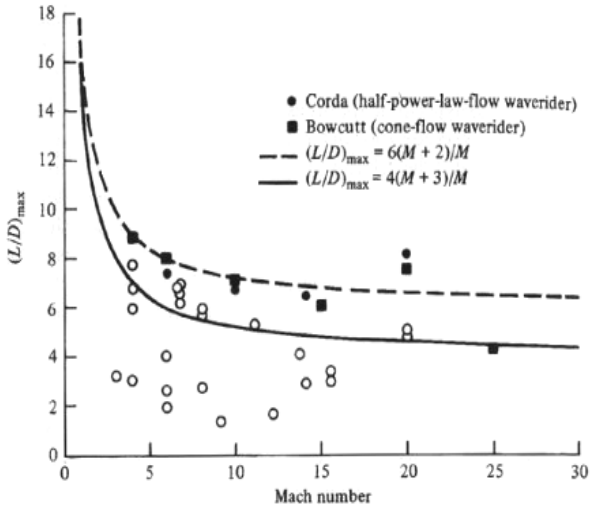

Figure 2: The Kuchemann "L/D barrier" and Waverider Performance

Further, the goal of this paper seeks to develop a design methodology for the creation of waverider configurations, and identify the engineering parameters that influence their aerothermodynamic performance and to provide an answer to the following problem: a supersonic flow interacts with a shockwave and it is required that a numerical process be defined to construct the geometric shapes or waveriders that support the generating shockwave.

From a fluid dynamic point of view, this study is concerned with the creation of a class of hypersonic vehicle configurations with superior performance that satisfies the coupled Euler equations and their appropriate boundary conditions for a predetermined flight altitude, flight speed and vehicle dimension. Once an appropriate class hypersonic vehicle configuration is determined, engineering design parameters are sought, identified and manipulated in a manner that improves the overall efficiency of the resulting waverider.

II. DESIGN METHODOLOGY

The design process described in this research is based on the work done in Refs. 5-7, and which is built on the following two axioms: First, two imaginary streamlines are assumed to

emanate from each point on the shock surface. One represents a freestream streamline that is processed by the shock and another, which remains undisturbed, as shown in Figure 3. Any curve described on the generating shockwave will be called a leading edge. Each leading edge generates an upper freestream surface and a lower compression surface.

Secondly, the inviscid surfaces are replaced by a solid wall without any interference to the outer flowfield. Using these axioms, the generation of a particular configuration becomes a matter of choosing appropriate leading edges on an assumed shockwave surface. The waverider design process is illustrated in Figure 3. It is of interest to note that in constructing waveriders the choice of leading edges is of utmost importance. As illustrated in Figure 3, a choice of one leading edge will result in a wedge, whereas another leading edge on the very same shockwave will result in a caret waverider and a third results in a generic waverider.

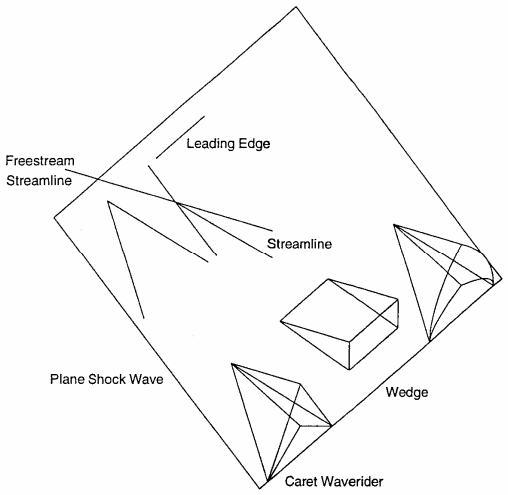

Figure 3: Illustration of Waverider Construction from Oblique Shockwaves

II. A. FLOWFIELD GENERATION

An integral part of the waverider design is the flowfield information behind a shockwave of interest, as the waverider is a product of its environment. The methodology developed in Refs. 5-7 is used to generate, conical, hypersonic flowfields from which waveriders are carved and this design method is applicable to two-dimensional, axisymmetric and generalized three-dimensional flowfields. In an effort to describe this tool without undue complexity, a complete analysis is given here of the flowfield generated by an arbitrary axisymmetric shock shape.

In the following three sections, all numerical processes will be described in a cylindrical coordinate frame of reference, namely, x, r and ϕ, where the x axis is aligned with the free stream velocity vector. The flow variables are the properties of the flowfield, namely u, v, p and ρ, where ρ is the density, u and v the cylindrical velocity components in the x and r directions respectively, and p the pressure.

II. B. HYPERSONIC FLOWFIELD CONSTRUCTION

Given the Mach number and altitude, the freestream properties are known. The arbitrary shockwave shape is described in the form:

$$\begin{aligned} r_{1,j} &= f(x_{1,j}) \\ x_{1,j+1} &= x_{1,j} + \delta x \end{aligned} \tag{1}$$

and defined in the interval *(a, b),* where $\delta x = (b - a)/N$. Each point numbered *j;* for $j = 1, N + 1$ and $i = 1$, represents the beginning of a streamline on the shockwave. In addition, a line described by *i*, for $i = const$, will be called a data line. The flow variables and their respective partial derivatives at each point on a given data line must be found. This information is used in a Taylor series expansion to predict the flow parameters on a new data line some distance *dx* and *dr* downstream in the flowfield. However, the increments, *dx* and δx, represent two different intervals, the first being an increment in the development of the flowfield and the second, an increment along the shockwave. In this study, *dx* is chosen to be half of δx.

The first data line, along which the flowfield information is known, is immediately after the shockwave, and can be represented by the shockwave itself for the sake of simplification. The objective of the numerical process thereafter is to develop a new data line some distance *dx* and *dr* downstream. In general, the increment, *dx*, may be chosen as a constant value through out the flowfield. However, the increment, *dr*, must be calculated at each grid point. The new flowfield parameters: *u*, *v*, *p* and ρ are evaluated as per the Taylor Series expansion formulation as follows using m to represent any flowfield parameter:

$$m_{i+1,j} = m_{i,j} + \frac{\partial m}{\partial x} dx + \frac{\partial m}{\partial r} dr_{i,j} \tag{2}$$

Similarly, the new grid point locations are evaluated as follows:

$$\begin{aligned} x_{i+1,j} &= x_{i,j} + dx \\ r_{i+1,j} &= r_{i,j} + dr_{i,j} \end{aligned} \tag{3}$$

The values for dr used in equations 3 are evaluated as follows:

$$dr_{i,j} = \frac{v_{i,j}}{u_{i,j}} dx \tag{4}$$

The data illustrated in equations 2 and 3 represents a new data line along which all the flowfield parameters are known. However, this line is developed from a forward marching technique and therefore has one less data point, as shown in Figure 4.

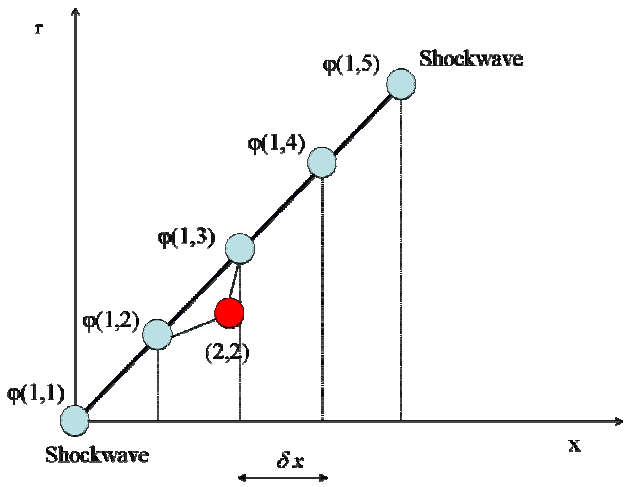

Figure 4: Creating Next Data Point

The next challenge is the development of the partial derivatives, $\frac{\partial u}{\partial r}, \frac{\partial v}{\partial r}, \frac{\partial \rho}{\partial r}, \frac{\partial p}{\partial r}, \frac{\partial u}{\partial x}, \frac{\partial v}{\partial x}, \frac{\partial \rho}{\partial x}$, *and* , $\frac{\partial p}{\partial x}$, used in the evaluation of the updated flow variables defined in equations 2. The Euler equations, described in the form,

$$u\frac{\partial \rho}{\partial x} + \rho\frac{\partial u}{\partial x} + \rho\frac{\partial v}{\partial r} + v\frac{\partial \rho}{\partial r} = -\frac{\rho v}{r} \tag{5}$$

$$u\frac{\partial u}{\partial x} + v\frac{\partial u}{\partial r} + \frac{1}{\gamma \rho M_\infty^2}\frac{\partial p}{\partial x} = 0 \tag{6}$$

$$u\frac{\partial v}{\partial x} + v\frac{\partial v}{\partial r} + \frac{1}{\gamma \rho M_\infty^2}\frac{\partial p}{\partial r} = 0 \tag{7}$$

$$u\frac{\partial P}{\partial x} + v\frac{\partial P}{\partial r} - \frac{\gamma P u}{\rho}\frac{\partial \rho}{\partial x} - \frac{\gamma P v}{\rho}\frac{\partial \rho}{\partial r} = 0 \tag{8}$$

where equations 5 – 8 are the continuity, x momentum, y momentum, and energy equations respectively. These equations are coupled to the directional derivatives of the flow parameters along a given data line, in the form,

$$\frac{\partial u}{\partial x}\frac{dx}{d\ell} + \frac{\partial u}{\partial r}\frac{dr}{d\ell} = \frac{du}{d\ell} \tag{9}$$

$$\frac{\partial v}{\partial x}\frac{dx}{d\ell} + \frac{\partial v}{\partial r}\frac{dr}{d\ell} = \frac{dv}{d\ell} \tag{10}$$

$$\frac{\partial \rho}{\partial x}\frac{dx}{d\ell} + \frac{\partial \rho}{\partial r}\frac{dr}{d\ell} = \frac{d\rho}{d\ell} \tag{11}$$

$$\frac{\partial p}{\partial x}\frac{dx}{d\ell} + \frac{\partial p}{\partial r}\frac{dr}{d\ell} = \frac{dp}{d\ell} \tag{12}$$

that represents a closed set of algebraic equations of eight equations and eight unknowns relative to the eight partial derivatives, $\frac{\partial u}{\partial r}, \frac{\partial v}{\partial r}, \frac{\partial \rho}{\partial r}, \frac{\partial p}{\partial r}, \frac{\partial u}{\partial x}, \frac{\partial v}{\partial x}, \frac{\partial \rho}{\partial x}$, *and* , $\frac{\partial p}{\partial x}$. Further, equations 5 – 12 are coupled into a linear algebraic equation matrix Ax=B, where:

$$A = \begin{pmatrix} \rho & 0 & 0 & \rho & u & v & 0 & 0 \\ u & v & 0 & 0 & \frac{1}{\gamma \rho M_\infty^2} & 0 & 0 & 0 \\ 0 & 0 & u & v & 0 & \frac{1}{\gamma \rho M_\infty^2} & 0 & 0 \\ 0 & 0 & 0 & 0 & \frac{-\gamma P u}{\rho} & \frac{-\gamma P u}{\rho} & u & v \\ \frac{dx}{dL} & \frac{dy}{dL} & 0 & 0 & 0 & 0 & 0 & 0 \\ 0 & 0 & \frac{dx}{dL} & \frac{dy}{dL} & 0 & 0 & 0 & 0 \\ 0 & 0 & 0 & 0 & \frac{dx}{dL} & \frac{dy}{dL} & 0 & 0 \\ 0 & 0 & 0 & 0 & 0 & 0 & \frac{dx}{dL} & \frac{dy}{dL} \end{pmatrix} \tag{13}$$

where matrix A represents the portion that includes both Euler's equations and the directional derivatives,

$$x = \begin{pmatrix} \partial u/\partial x \\ \partial u/\partial y \\ \partial v/\partial x \\ \partial v/\partial y \\ \partial \rho/\partial x \\ \partial \rho/\partial y \\ \partial P/\partial x \\ \partial P/\partial y \end{pmatrix} \tag{14}$$

where matrix x is the unknown matrix,

$$B = \begin{pmatrix} -\rho v / r \\ 0 \\ 0 \\ 0 \\ du/dL \\ dv/dL \\ d\rho/dL \\ dP/dL \end{pmatrix} \tag{15}$$

and matrix B is the product of matrix A times matrix x. This is solved analytically using Mathematica, Ref. 8 to yield the following solutions,

$$\left(\frac{\partial \varphi}{\partial x}\right)_{i,j}^{k} = f(u, v, \rho, p, M, \gamma)_{i,j:i,j+1} \tag{16}$$

where the index *k, k = 1, 8* and represents the following eight partial derivatives, $\frac{\partial u}{\partial r}, \frac{\partial v}{\partial r}, \frac{\partial \rho}{\partial r}, \frac{\partial p}{\partial r}, \frac{\partial u}{\partial x}, \frac{\partial v}{\partial x}, \frac{\partial \rho}{\partial x}$, *and* $, \frac{\partial p}{\partial x}$.

The new data line will be described *by i* = 2, along which *j* ranges from 1 through N. This data line becomes the initial data line for *j; j = 1, N+1-i* and *i = i+1*. The numerical process is then repeated until *i = N+1*. Figure 5 shows the triangular grid system developed in this process.

II. C. FLOWFIELD CALCULATIONS

With the Mach number, altitude, freestream quantities, and shockwave shape prescribed, the local shockwave relations, described in Ref. 9, are used to evaluate the flow variables across the shockwave and on each point on the first data line, *i =1,* and *j =1, N+1.* Using the approach explained in section 2.1, the partial derivatives of the flowfield variables, namely; $\frac{\partial u}{\partial r}, \frac{\partial v}{\partial r}, \frac{\partial \rho}{\partial r}, \frac{\partial p}{\partial r}, \frac{\partial u}{\partial x}, \frac{\partial v}{\partial x}, \frac{\partial \rho}{\partial x}$, and $\frac{\partial p}{\partial x}$ are evaluated on each point on the data line, *i =1,* and *j =1, N* using the expressions,

$$\left(\frac{\partial \varphi}{\partial x}\right)_{i,j}^{k} = f(u, v, \rho, p, M, \gamma)_{i,j:i,j+1} \tag{17}$$

Because the directional derivatives require information from two points on the data line, it is possible only to obtain the derivatives for *j = 1, N*. Thus, the second data line will be one point shorter than the first.

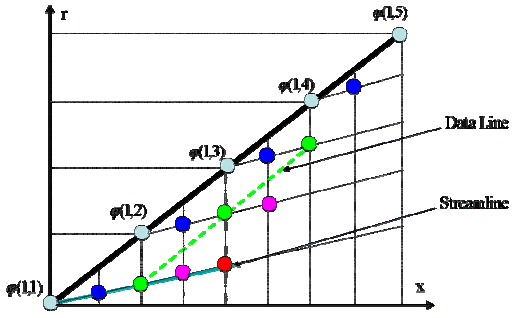

Figure 5: Triangular Grid

Next, the flowfield parameters are evaluated at the next set of grid points on the new data line, i.e., *i = 2, j = 1, N*, through the use of the Taylor series expansion,

$$\varphi_{i+1,j} = \varphi_{i,j} + \frac{\partial \varphi}{\partial x} dx + \frac{\partial \varphi}{\partial r} dr_{i,j} \tag{18}$$

where the function, φ, represents any one of the flowfield variables, mainly u, v, ρ and p. It is of interest to note that once the new flowfield variables are evaluated, the physical location of the grid points may be updated as follows:

$$dr_{i,j} = \frac{(v_{i+1,j} + v_{i,j})}{(u_{i+1,j} + u_{i,j})} dx \tag{19}$$

This process is repeated for the remaining data lines (*i = 3, N+1)* as well, with each one being one point shorter than the one before it, which leads to the triangular shape of the grid in Figure 5. With this numerical approach, a particular streamline is traced by holding the index, *j*, fixed and the index, *i*, varied, such that, *i = 1, N+1-j*, as shown in Figure 5.

II. D. LOCAL SKIN FRICTION COEFFICIENT AND SHEAR STRESS CALCULATIONS

The skin friction coefficient distribution along the streamlines that form the waverider configuration is evaluated using the reference temperature method, Ref. 4. For laminar flow, the local skin friction is given by:

$$c_f = \frac{0.664}{\sqrt{\mathrm{Re}_s}} \left(\frac{T'}{T_\infty} \right)^{(\omega-1)/2} \tag{20}$$

where Re_s is the local Reynolds number as defined as:

$$\mathrm{Re}_s = \frac{\rho_\infty v_\infty s}{\mu_\infty} \tag{21}$$

where v_∞, μ_∞ and ρ_∞ are freestream quantities and *s* is the local distance measured from the leading edge. The reference temperature *T'* is calculated as follows:

$$\frac{T'}{T_\infty} = 1.0 + 0.32 M_\infty^2 + 0.58 \left(\frac{T_w}{T\infty} - 1 \right) \tag{22}$$

where M_∞ is the freestream Mach number and T_w is the wall temperature. The exponent ω used in equation 20 is the exponent in the approximate viscosity variation relationship, namely,

$$\frac{\mu'}{\mu} = \left(\frac{T'}{T_\infty} \right)^\omega . \tag{23}$$

In this research, the value of ω was set to 0.75. In the case of turbulent flow, the local skin friction is evaluated in accordance with the relationship given as:

$$c_f = \frac{0.0592}{\left(\mathrm{Re}'_s\right)^{0.2}} \tag{24}$$

where:

$$\mathrm{Re}'_s = \frac{\rho' v_\infty s}{\mu'} . \tag{25}$$

The quantities ρ' and μ' are evaluated at the reference temperature defined in equation 22. The local shear stress is found to be a function of the skin friction coefficient and is calculated with this equation:

$$\tau = C_f * q_E \tag{26}$$

where q_E is the dynamic pressure at the edge, defined by:

$$q_E = \frac{1}{2} \rho * V^2 \tag{27}$$

The effects of boundary layer transition on the skin friction coefficient and the shear stress are shown by Figure 9. Boundary layer transition is predicted using the correlation given by Bowcutt, Ref. 2. This relationship is expressed as a function of the edge Mach number, M_e in the following manner:

$$\log \mathrm{Re}_s = 6.421 \exp\left(1.209 \times 10^{-4} M_e^{2.641}\right) \tag{28}$$

where Re_s is the transition Reynolds Number. In this research, the transition region was not considered, simplifying into a transition point.

II. E. LOCAL HEAT TRANSFER EVALUATIONS

It has been well established that for hypersonic, two-dimensional, zero pressure gradient, laminar boundary layers; the intermediate enthalpy method provides a good method of prediction. However, the experimental work done by East and Baxter, Ref. 10 was instead used to evaluate the local heat transfer rate on the solid streamlines. The local heat transfer rate, $\dot{q}_w$ for laminar boundary layers is evaluated using a correlation, Ref. 11 between the Stanton number St' and Reynolds number Re' given as:

$$St' = 0.332 \, \mathrm{Pr}^{-2/3} \, \mathrm{Re}'^{-1/2}_s \tag{29}$$

where

$$St' = \frac{\dot{q}_w}{\rho' v_e \left(h_e - h_w\right)} \tag{30}$$

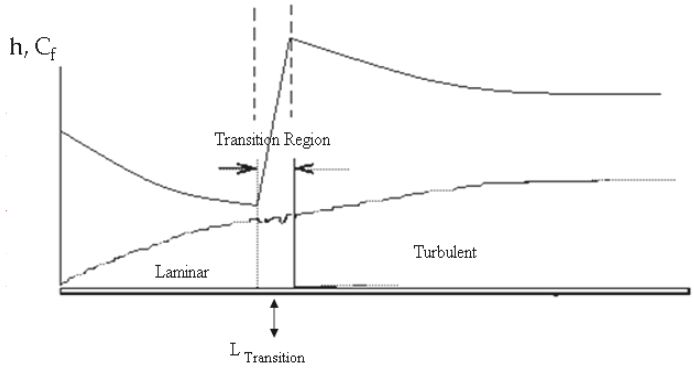

Figure 6: Boundary Layer Transition

For turbulent boundary layers, the heat transfer rate was calculated using the relationship given by Wieghardt, Ref. 10, as follows:

$$St' = 0.176\left(\log_{10} \mathrm{Re}'_s\right)^{-2.45} \tag{31}$$

The numerical value used for Pr is 0.71 for laminar flow.

III. SHAPE GENERATION

Now that the flowfield is constructed and the streamlines extracted, a three-dimensional waverider can now be created. In order to create a three-dimensional waverider from a two-dimensional flowfield, a third dimension, or Z, must be added. Any shape can be created with the appropriate set of Z-coordinates. In the case of an axisymmetric flowfield, the coordinates are found with the use of the waverider shape angle, ϕ_j. With the x and r coordinates from the flowfield, the shape angle can be used to create any number of different shapes.

III. A. WAVERIDER SHAPE ANGLE

The shape of the waverider is defined in cylindrical coordinates, *x*, *r*, and ϕ_j, where the x-axis is along the waverider's length. In order to make the shape three-dimensional, the *r* coordinates need to be rotated by the angle ϕ_j. The shape angle, ϕ_j is defined by choosing a base plane curve, as shown in Figure 7, with $j = 1, N+1$. Once a base curve is chosen and a set of shape angles found, the waverider shape is carved from the conical flowfield, as shown in Figures 8 and 9.

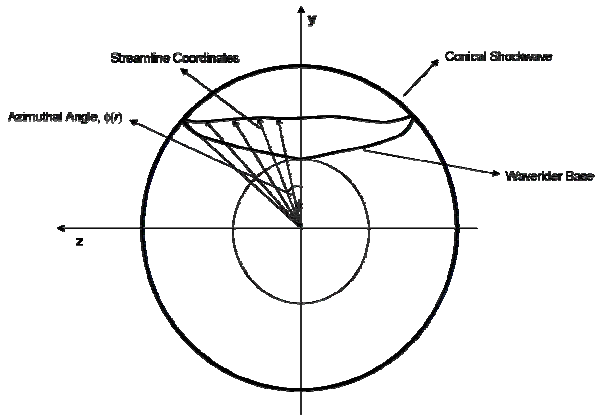

Figure 7: Base Plane

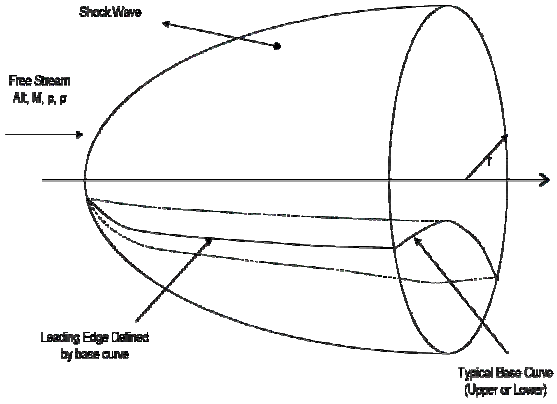

Figure 8: Conical Flowfield and Base Curve

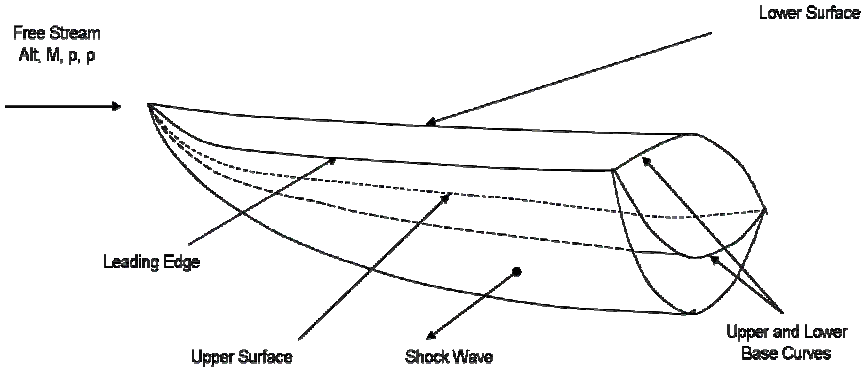

Figure 9: Completed Waverider Forebody

III. B. WAVERIDER EXAMPLES

In this study, twenty-three different waverider shapes were created. Each one used the same x and r coordinates. However, each had its own unique set of shape angles. Two of them, a flat top waverider and a flat bottom waverider, are offered as examples. All twenty-three shapes, and their data, can be found in the Appendix.

In order to create a flat top waverider (Figure 10), the base curve would be described by a set of shape angles defined by:

$$\phi_j = \arccos\left(\frac{r^u_{N+1,1}}{r^u_{N+1,j}}\right) \tag{32}$$

Similarly, a flat bottom waverider (Figure 11) may be described by the expression,

$$\phi_j = \arccos\left(\frac{r^l_{N+1,1}}{r^l_{N+1,j}}\right) \tag{33}$$

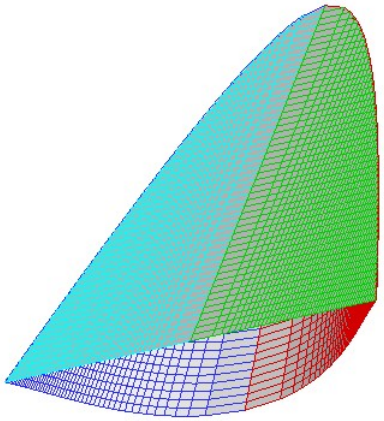

Figure 10: Flat Top Waverider

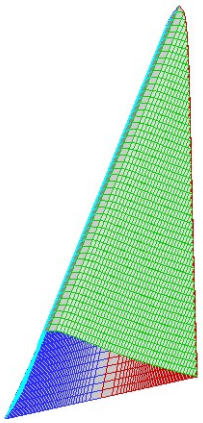

Figure 11: Flat Bottom Waverider

The flow variables and viscous properties found before are independent from the actual shape of the waverider. However, they are indeed the properties found along the upper and lower surfaces of the waverider. Figure 12 shows the density distribution along the lower surface of a flat top waverider (inverted as to give a better view of the lower surface). Also, it shows a slice of the flowfield along the middle, and another slice at the base to show that the density distribution of the flowfield matches that on the lower surface.

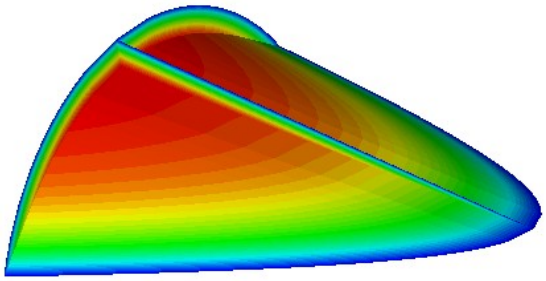

Figure 12: Density Distribution along Lower Surface of Flat Top Waverider

IV. AERODYNAMIC ANALYSIS

With the waverider shape completed, it is possible to perform an aerodynamic analysis. It being an aircraft, it is very important to determine its aerodynamic properties such as lift and drag. Such an analysis is possible due to the waverider simulation using actual dimensions for the coordinates. Aerodynamic forces and moments are calculated by numerically integrating the local pressures and shear stresses acting on the waverider wetted surfaces. The mean value theorem is used to evaluate all surface integration routines.

IV. A. THE MEAN VALUE THEOREM

The evaluation of the inviscid force on a given waverider configuration involves the evaluation of the following expressions as they are applied to the upper and lower waverider surfaces,

$$\vec{F} = \oiint_{waverider} P d\vec{S} \tag{34}$$

and

$$\vec{F}_P = D_P\vec{i} + L_P\vec{j} + G_P\vec{k} \tag{35}$$

where D_p, L_p, and S_p are the Lift, Drag, and Slip forces due to pressure and dS is defined as:

$$d\vec{S} = dS_x\,\vec{i} + dS_y\,\vec{j} + dS_z\,\vec{k} \tag{36}$$

with S_x, S_y, and S_z being the area projections onto the yz, xz, and xy planes respectively, as shown in Figure 13.

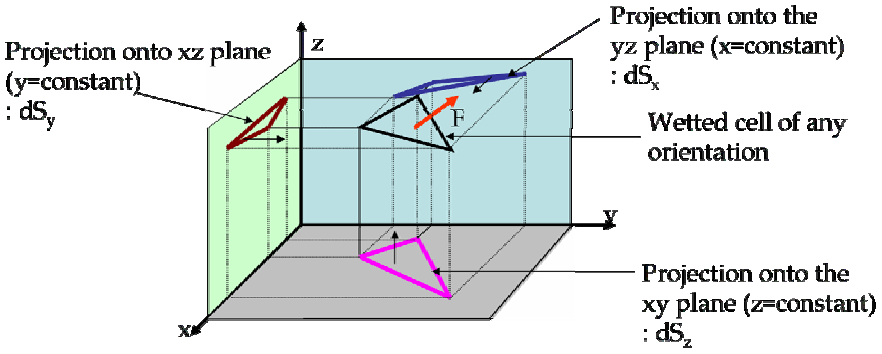

Figure 13: Projected Areas

Similarly, the force due to shear stress is evaluated with the following expressions,

$$\vec{F} = \oiint_{waverider} \tau d\vec{S} \tag{37}$$

$$\vec{F}_\tau = D_\tau\vec{i} + L_\tau\vec{j} + G_\tau\vec{k} \tag{38}$$

Using the mean value theorem, equations 34, 36, and 37 become:

$$\begin{aligned}\vec{F}_p &= \oiint_{waverider} p d\vec{S} = p_{avg} \oiint_{waverider} d\vec{S} = p_{avg} \oiint_{waverider} \left(dS_x\,\vec{i} + dS_y\,\vec{j} + dS_z\,\vec{k}\right) \\ \vec{F}_\tau &= \oiint_{waverider} \tau d\vec{S} = \tau_{avg} \oiint_{waverider} d\vec{S} = \tau_{avg} \oiint_{waverider} \left(dS_x\,\vec{i} + dS_y\,\vec{j} + dS_z\,\vec{k}\right)\end{aligned} \tag{39}$$

IV. B. PROJECTED AND WETTED AREAS

In order to evaluate equation 37, first the area projections must be calculated. The waverider shapes are often not shapes of which the area can be easily taken. Therefore the Triangulation Method is used. With the Triangulation Method, the surface of the waverider is divided into many triangle-shaped elements. Figure 14 shows a single element ABC.

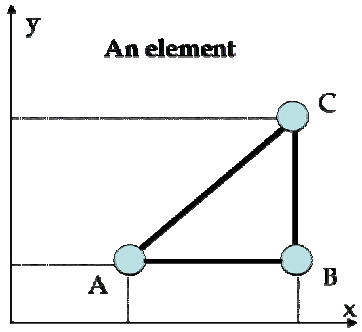

Figure 14: Example Element

The sides of the element are calculated as follows:

$$\begin{aligned} AB &= \left\{\lambda_x\left(X_A - X_B\right)^2 + \lambda_y\left(Y_A - Y_B\right)^2 + \lambda_z\left(Z_A - Z_B\right)^2\right\}^{0.5} \\ AC &= \left\{\lambda_x\left(X_A - X_C\right)^2 + \lambda_y\left(Y_A - Y_C\right)^2 + \lambda_z\left(Z_A - Z_C\right)^2\right\}^{0.5} \\ BC &= \left\{\lambda_x\left(X_B - X_C\right)^2 + \lambda_y\left(Y_B - Y_C\right)^2 + \lambda_z\left(Z_B - Z_C\right)^2\right\}^{0.5} \end{aligned} \tag{40}$$

where λ_m equals 1 or 0 if the projection is in the m direction. The projected area is calculated with these expressions:

$$\begin{aligned} t &= (AB + BC + AC)/2 \\ A_{element} &= \left(t*(t-AB)*(t-BC)*(t-AC)\right)^{0.5} \\ S_m &= \sum\sum A_{element} \end{aligned} \tag{41}$$

For the average shear stress calculations, the wetted areas can also be calculated with equations 40 and 41, keeping $\lambda = 1$.

IV. C. AVERAGE PRESSURE AND SHEAR STRESS

The final unknowns in equations 39 are the average pressure and average shear stress. The average pressure is simply calculated as:

$$P_{avg} = \frac{\sum_j \sum_i P_{i,j}}{\sum_j \sum_i i,j} \tag{42}$$

In order to calculate the average shear stress, a triangular element is once again used (see Figure 14). First, the average force due to shear stress on each element is calculated in the following manner:

$$f_{avg}^{element} = \frac{(\tau_A + \tau_B + \tau_C)}{3} * A \tag{43}$$

where A is the wetted area of the element. Then, the average shear stress is calculated

$$\tau_{avg} = \frac{\sum\sum f_{avg}^{element}}{\text{T}otal\ wetted\ area} \tag{44}$$

IV. D. LIFT, DRAG, AND SIDE FORCES

Each variable in equations 39 are now known and thus the forces on the waverider can be evaluated. Keeping in mind that the Lift is the j component, the Drag the i component, these forces are evaluated as:

$$\begin{aligned} L &= P_{avg} A_{Plan} - \tau_{avg} A_{Base\_View} \\ D &= P_{avg} A_{Base} + \tau_{avg} A_{Plan\_View} \end{aligned} \tag{45}$$

where A_{Plan} is the plan form area, A_{Base} is the base area, and A_{Base_View} and A_{Plan_View} are the projections of the base and planform areas. The Side Force is neglected due to the symmetrical design of the waverider, which causes the Side Forces to cancel each other out. Other aerodynamic properties are found with these equations:

$$\begin{aligned} C_L &= \frac{L}{q_\infty A_{Plan}} \\ C_D &= \frac{D}{q_\infty A_{Plan}} \end{aligned} \tag{46}$$

V. CODE VALIDATION AND RESULTS

V. A. CODE VALIDATION

In order for the results of a code to be meaningful, they have to be validated. Otherwise, the results are a group of meaningless numbers. To validate this code, the results are compared to two other waverider generation codes developed by the University of Maryland (UMD) and Dr. Ferguson (Old Code), Ref. 7 with a Mach number of 6, waverider length of 1 m, and shockwave angle of 16° for a Flat Top Waverider at sea level in Table 1.

Table 1. Comparison of Code to Previous Codes

	UMD	Old Code	New Code	% Error
Geometric Properties				
Base Height/Length	0.1734	0.1800	0.1737	-1.7068
Semi-span/Length	0.4968	0.4969	0.4887	-1.6381
Volumetric Efficiency	0.1868	0.1967	0.2015	5.0691
Base Area (m^2)	0.1050	0.1117	0.1054	-2.7365
Planform Area (m^2)	0.6158	0.6155	0.6038	-1.9258
Total Wetted Area (m^2)	1.2679	1.2717	1.2458	-1.8901
Volume (m^3)	0.0390	0.0421	0.0424	4.6303
Aerodynamic Properties				
C_D	0.0196	0.0191	0.0187	-3.5003
C_L	0.0914	0.0942	0.0857	-7.6584
L/D	4.6691	4.9392	4.5294	-5.7189

With the exception of C_L, the results of the new code have stayed very close to those of the previous two codes.

Figure 15 shows the shear stress distribution in the lower and upper surfaces with a Mach number of 10, waverider length of 10 m, and a shockwave angle of 16°. The behavior of the shear stress is as expected, with the shear stress in the lower surface being much higher than that in the upper. Also, this shows that most of the waverider is in the turbulent region, which is also expected.

Figure 16 shows the velocity distribution in the flowfield on the upper and lower surfaces. On the lower surface, the velocity is the highest just after the shockwave. Then, the velocity drops as the flowfield goes further away from the shockwave. The upper surface, however, has a constant velocity due to not coming into direct contact with the shockwave.

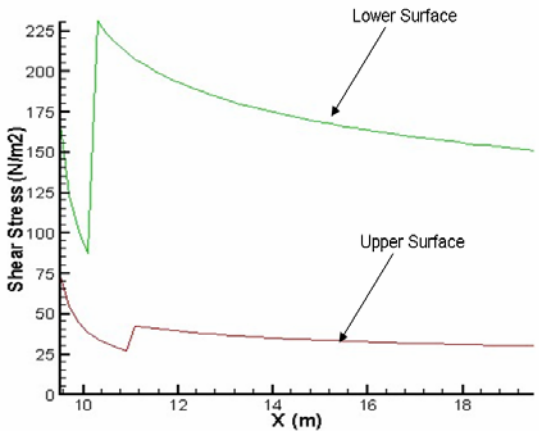

Figure 15: Shear Stress Distribution

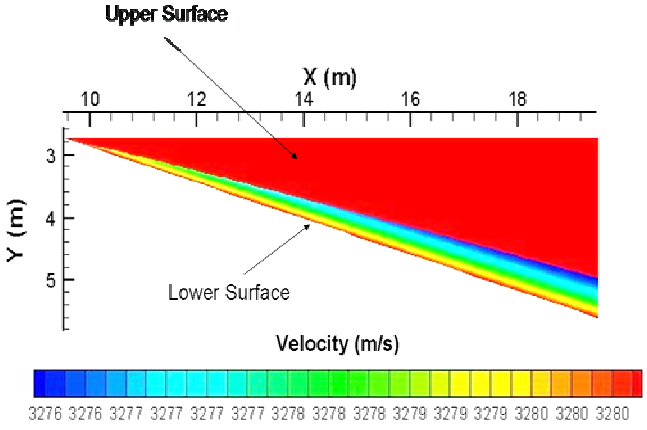

Figure 16: Velocity Distribution through the Flowfield

V. B. CODE VALIDATION

Each of the waverider configurations developed with this code has an acceptable L/D. The Kuchemann Barrier (Figure 2) is considered to represent the best performance possible at high Mach Numbers. The waverider configurations developed with this code each achieved an L/D that was close to the Kuchemann Barrier, if not higher. Figure 17 shows how the Flat Bottom, Lower Circular Arc, and Bat Wing waveriders compares to the Kuchemann Barrier using a waverider length of 10 and a shockwave angle of 14°.

Figure 18 shows the shear stress distribution along the lower surface of the Flat Top waverider. The shear stress decreases as it gets further away from the edge. However, the shear stress at the edge is not the highest as it would be expected to be.

Table 2 shows the aerodynamic properties, as well as volume, surface area, and volumetric efficiency of all twenty-three waverider configurations. The highest L/D was achieved by the Lower Circular Arc Waverider, with an L/D of 4.7527. The highest volumetric efficiency was also achieved by the Lower Circular Arc Waverider, with a volumetric efficiency of 0.78243.

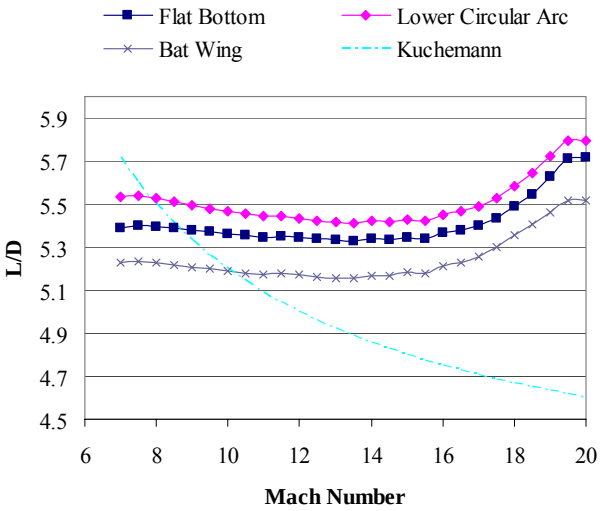

Figure 17: Lift Over Drag Comparison

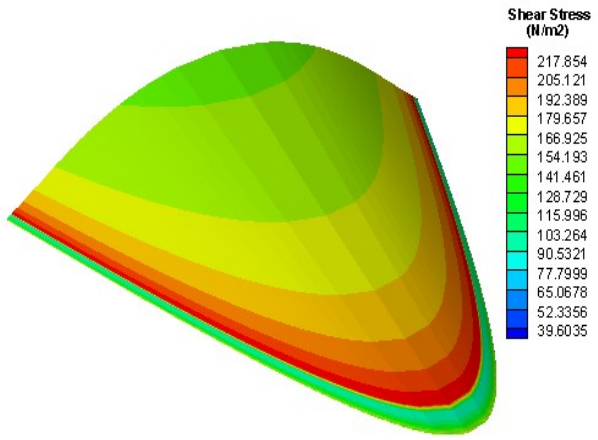

Figure 18: Shear Stress Distribution on Flat Top Lower Surface

Table 2. Waverider Data

Shape	CL	L/D	CD	Volume (m^3)	Surface Area (m^2)	V_{eff}
1	0.11209	4.2269	0.02652	58.0565	129.4860	0.24371
2	0.11214	4.6640	0.02404	25.9711	64.9136	0.31847
3	0.11211	4.4480	0.02521	43.9381	101.6120	0.25527
4	0.11214	4.7016	0.02385	22.2308	56.6178	0.36306
5	0.11210	4.3673	0.02567	51.4181	114.4620	0.25128
6	0.11214	4.7089	0.02381	21.6389	55.0574	0.37701
7	0.11219	4.7452	0.02364	17.2617	44.7753	0.56823
8	0.11214	4.7443	0.02637	16.3763	43.9595	0.55101
9	0.11210	4.3572	0.02573	52.1933	115.8680	0.25085
10	0.11210	4.6850	0.02393	24.1043	60.6333	0.33896
11	0.11212	4.4672	0.02510	46.3150	102.7520	0.26229
12	0.11214	4.7124	0.02380	21.2789	54.2127	0.38475
13	0.11218	4.5645	0.02458	38.8586	85.8081	0.29698
14	0.11214	4.7527	0.02360	15.1446	40.6014	0.78243
15	0.11212	4.4888	0.02498	46.0558	101.1490	0.26654
16	0.11214	4.6914	0.02390	24.2491	60.1120	0.34770
17	0.11212	4.4689	0.02509	46.5669	102.9180	0.26296
18	0.11214	4.6956	0.02388	23.1596	58.3632	0.35335
19	0.11210	4.3173	0.02597	54.0409	120.1740	0.24805
20	0.11214	4.6818	0.02395	24.3969	61.2937	0.33550
21	0.11214	4.6769	0.02398	29.9306	68.5911	0.33878
22	0.11214	4.7469	0.02362	16.3591	43.4303	0.58429
23	0.11212	4.5248	0.02478	28.2423	79.5796	0.26466

M=10.0 ß=16.0 Length =10.0

V. C. CONCLUSIONS AND RECOMMENDATIONS

Using this methodology, twenty-three different shapes were designed. All twenty-three used the same flowfield, the same conditions, and the same *x* and *r* coordinates. The only difference in their design was the set of shape angles used, which shows that any shape is possible with this method. Also, each waverider achieved L/D that stayed close to the Kuchemann Barrier, sometimes even crossing it. However, these waverider shapes are only forebodies. A complete waverider configuration, adding a combustor and nozzle, should increase the L/D even further.

In this research, the effects of blunting were not considered. The waveriders designed with this method all have sharp edges. In further studies, the effects of blunting should be explored and should in turn reduce the errors in the shear stress and L/D calculations.

VI. REFERENCES

[1]Kuchemann, D. The Aerodynamic Design of Aircraft, Oxford, Pergamon, 1978.

[2]Bowcutt, Kevin G., Anderson, John D., Jr., and Capriotti, Diego. Viscous Optimized Hypersonic Waveriders, AIAA Paper 87-0272, 1987.

[3]Corda, Stephen and Anderson, John D., Jr. Viscous Optimized Waveriders Designed from Axisymmetric Flowfields, AIAA Paper 88-0369, 1988.

[4]Anderson, John D., Jr. Introduction to Flight, 4th ed. Boston: McGraw-Hill, 2000, pp. 622-626 and 681-707.

[5]Ferguson, Frederick, Ph. D Dissertation, Department of Aerospace Engineering, University of Maryland, College Park, Maryland, UM-AERO-93-5. 1993.

[6]Ferguson, Frederick, et al., A Design Method for the Construction of Hypersonic Vehicle Configurations, AIAA 95-6009, Chattanooga, TN, April 3-7, 1995.

[7]Ferguson, Frederick, and John D. Anderson, Jr., Expanding the Waverider Design Space Using General Supersonic and Hypersonic Generating Flows, AIAA 93-0505, Reno, NV, January 11-14, 1993.

[8]Wolfram, Stephen. Mathematica: A System of Doing Mathematics by Computer, Addison-Wesley Publishing Company, Inc., 1991.

[9]Anderson, John D. Jr., Fundamentals of Aerodynamics, McGraw-Hill Book Co., New York, 1984.

[10]East, R.A., and Baxter, D.R.J., Comparative Heat Transfer Measurements on Caret and Flat Compression Surfaces for Hypersonic Intakes, 1st International Hypersonic Waverider Symposium, October, 1990.

[11]Eckert, E.R.G., Engineering Relations for Heat Transfer and Friction in High Velocity Laminar and Turbulent Boundary Layer Flow Over Surfaces With Constant Pressure and Temperature, ASME Vol. 78, No. 6, August, 1956.